JACS Au
AN OPEN ACCESS JOURNAL OF THE AMERICAN CHEMICAL SOCIETY

pubs.acs.org/jacsau
Article

Electrocatalytic Ammonia Oxidation by a Ruthenium Complex Bearing a 2,6-Pyridinedicarboxylate Ligand

Published as part of JACS Au special issue "Advances in Small Molecule Activation Towards Sustainable Chemical Transformations".

Jun Li, Xiaohuo Shi, Feiyang Zhang, Xingyu Lu, Yaqiong Zhang, Rongzhen Liao,* and Biaobiao Zhang*

Cite This: JACS Au 2025, 5, 1812−1821
Read Online

ACCESS | Metrics & More | Article Recommendations | Supporting Information

ABSTRACT: Molecular catalysts for the electrocatalytic ammonia oxidation reaction (eAOR) have much to offer in terms of mechanistic investigations and practical energy issues. This work reports the use of complex [Ru(pdc-κ-N^1O^2)(bpy)(NH_3)] (**Ru-NH_3**) (H_2pdc = 2, 6-pyridinedicarboxylic acid; bpy = 2,2′-bipyridine) bearing a readily accessible pdc^{2-} ligand to catalyze ammonia oxidation under electrochemical conditions. The rich structural variations of **Ru-NH_3** in coordinating solvents and an ammonia atmosphere were fully characterized by cyclic voltammograms (CVs), NMR, and XRD. CV experiments showed that **Ru-NH_3** promotes electrocatalytic ammonia oxidation at a low overpotential of 0.85 V with a calculated catalytic rate (k_{obs}) of 18.9 s^{-1}. Controlled potential electrolysis (CPE) at an applied potential of 0.3 V vs $Fc^{+/0}$ achieves 76.1 equiv of N_2 with a faradaic efficiency of 89.8%. Experimental and computational analyses indicated that oxidation of **Ru-NH_3** generates a reactive **Ru^{III}-NH_3** intermediate, which undergoes sequential electron and proton transfer steps to form a **Ru^{VI}≡N** species. N−N bond formation occurs via the nucleophilic attack of an ammonia molecule on the **Ru^{VI}≡N** moiety with a facile barrier of 8.6 kcal/mol. Eventually, N_2 evolved as the product after releasing two electrons and three protons.

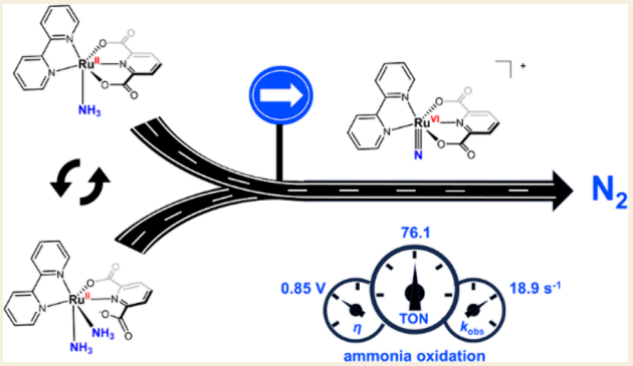

KEYWORDS: *ammonia oxidation, electrocatalysis, ruthenium, molecular catalyst, anionic ligand, carboxylate arm*

INTRODUCTION

As a carbon-free fuel, ammonia is an appealing candidate for addressing harmful CO_2 emissions and global energy demands because of its high energy density and transportability.[1,2] Catalytic ammonia oxidation to N_2 under electrochemical conditions has practical significance for developing direct ammonia fuel cells and utilizing ammonia as a hydrogen carrier.[3−5]

As a burgeoning research topic, studying homogeneous catalysts for ammonia oxidation has attracted increasing attention in recent years. A molecular-level understanding of ammonia oxidation provides several merits with respect to the mechanistic details and structure−activity relationships.[6,7] The challenge in catalyst development lies in overcoming the inherent stability of the N−H bonds of ammonia as well as the sluggish electron and proton transfers during N_2 formation. Transition metal-mediated N−H activation can take place when ammonia coordinates with the metal center. The magnitude of this activation relies on the nature of the metal and the coordination environment.[8]

Since Hamann et al. first demonstrated the electrocatalytic ammonia oxidation to 2.1 equiv of N_2 by a ruthenium complex in 2019,[9,10] numerous Mn-,[11] Fe-,[12−17] Ni-,[18] Cu-,[19,20] Mo-, and Ru-based molecular catalysts bearing different auxiliary ligands have been explored (Scheme 1).[21−31] To date, Berry and co-workers reported a diruthenium complex $Ru_2(chp)_4OTf$ (chp- = 6-chloro-2-hydroxypyridinate) with a lowest overpotential (∼0.7 V), but only 5 equiv of N_2 generated spontaneously.[25] Two excellent research works reported by Wang et al. and Warren et al. both achieved an overpotential under 0.8 V, while the conversion of ammonia to dinitrogen is finite.[14,20] Recently, Phearman and Bullock found that by modulating the electronic effects of the N-heterocyclic carbene ligands in an Fe-based catalyst, a 0.6 V shift in $Fe^{III}/^{II}$

Received: January 16, 2025
Revised: April 3, 2025
Accepted: April 3, 2025
Published: April 15, 2025

https://doi.org/10.1021/jacsau.5c00054
JACS Au 2025, 5, 1812−1821

Scheme 1. Representative Molecular Catalysts for Electrocatalytic Ammonia Oxidation[a]

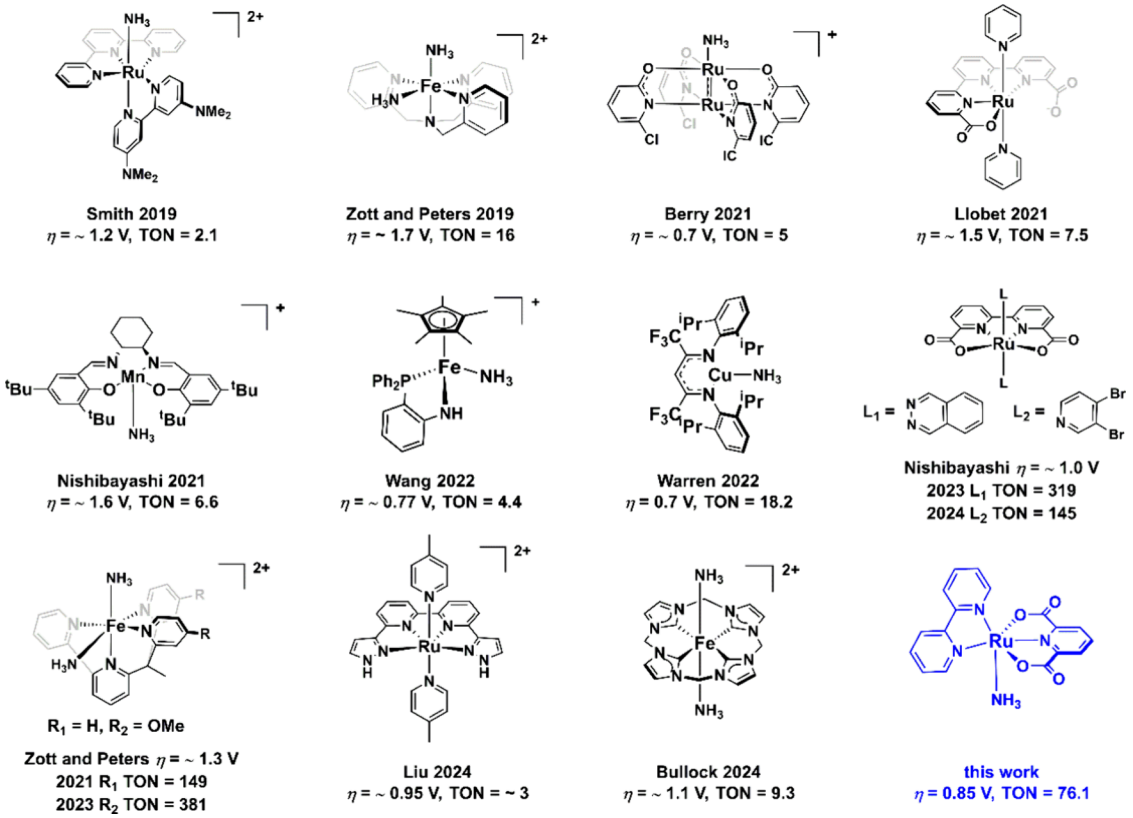

[a] η = overpotential of ammonia oxidation in organic solvents. TON = turnover number of N_2.

potential was observed.[16] Such a significant reduction in potential still results in no electrocatalytic performance of the catalyst, which indicated that simply reducing the redox potential has no positive effect on ammonia oxidation. In addition, Zott and Peters reported a series of works on an iron polypyridyl electrocatalyst for ammonia oxidation that exhibits an improved turnover number (TON) of N_2 from 16 to 149, and then to 381.[12,13,15] Unfortunately, this high TON was obtained at the expense of overpotential, meaning that ~1.3 V of overpotential is needed to drive the eAOR. By contrast, the catalyst with low overpotential and high TON is the Ru-bda (bda^{2-} = 2,2′-bipyridyl-6,6′-dicarboxylate) series reported by Nishibayashi and co-workers.[22,27,29] A TON of 145 can be achieved by optimizing substituents for axial pyridine ligands, and the TON is as high as 319 when phthalazines are used as axial ligands. Ménard and co-workers further reported the use of Ru-bda to electrocatalyze aqueous NH_3 to over 600 of N_2.[28] Moreover, when Llobet and co-workers loaded Ru-bda on the electrode surface, 7500 of TON could be obtained.[32] These studies show that the TON of ammonia oxidation can be greatly improved through the regulation of ligands and metals; however, developing ammonia oxidation catalysts with both low overpotential and high TON remains a challenge.

Herein, we report a new ammonia oxidation catalyst, $[Ru(pdc\text{-}\kappa\text{-}N^1O^2)(bpy)(NH_3)]$ (**Ru-NH$_3$**), which can promote eAOR at a low overpotential of 0.85 V with a TON of 9.4. Up to 76.1 equiv of N_2 can be generated at a higher applied potential of 0.3 V vs $Fc^{+/0}$. The presence of the anionic pdc^{2-} ligand increases the electron density on the Ru center, providing stability to the metal high oxidation states and lowering the overpotential of the reaction. Mechanistic investigation indicates that the N−N bond forms when ammonia attacks a **Ru^{VI}≡N** species, releasing N_2 as the final product.

RESULTS AND DISCUSSION

Synthesis and Characterization

As shown in Figure 1a, complex $[Ru(pdc\text{-}\kappa\text{-}N^1O^2)(bpy)(NH_3)]$ (**Ru-NH$_3$**) was prepared from complex $[Ru(pdc\text{-}\kappa\text{-}N^1O^2)(bpy)Cl]$ (**Ru-Cl**), which was synthesized according to the literature method,[33] by halide abstraction with $AgPF_6$ in aqueous ammonia solution. Crystallographic characterization of **Ru-NH$_3$** showed that the twisted bpy ligand with a torsion angle of 13.0(13)° was perpendicular to the pdc^{2-} ligand. The Ru−N3 bond length of 2.140(7) Å is consistent with the reported values of similar Ru^{II}−NH_3 complexes (Figure 1b). Due to the labile coordination of carboxylate groups of pdc^{2-}, **Ru-NH$_3$** can be completely converted into complex $[Ru(pdc\text{-}\kappa\text{-}N^1O^1)(bpy)(NH_3)_2]$ (**Ru-(NH$_3$)$_2$**) in the presence of excess ammonia and the latter can be transitioned back to **Ru-NH$_3$** after removal of ammonia (Figure 1a, for details, see the Supporting Information).

The carboxylate ligation in **Ru-NH$_3$** is also labile in coordinating solvents (Figure 1a). In DMSO, decoordination of the carboxylate arm of **Ru-NH$_3$** happened to form the complex $[Ru(pdc\text{-}\kappa\text{-}N^1O^1)(bpy)(NH_3)(DMSO)]$ (**Ru-(NH$_3$)(DMSO)**) (Figure S2). X-ray diffraction study of **Ru-(NH$_3$)(DMSO)** showed that solvent DMSO binds trans to the N4 atom of the pdc^{2-} ligand, and it has a distorted octahedral configuration: The N2−Ru−N3 angle is 96.50(15)°, and the

https://doi.org/10.1021/jacsau.5c00054
JACS Au 2025, 5, 1812−1821

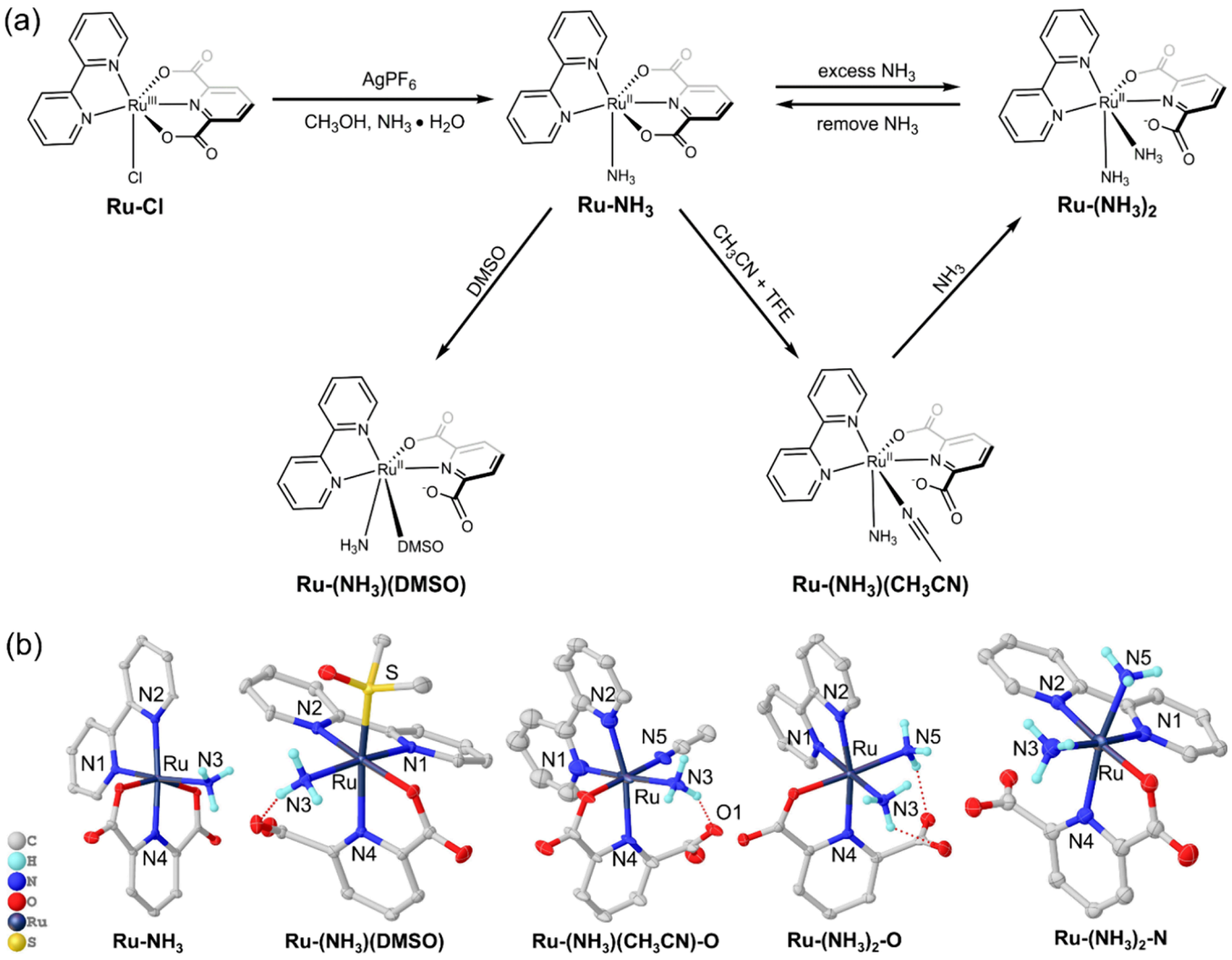

Figure 1. Synthesis and structure of complexes explored in this work. (a) Synthetic strategy for preparation of complex **Ru-NH$_3$**, **Ru-(NH$_3$)(DMSO)**, **Ru-(NH$_3$)(CH$_3$CN)**, and **Ru-(NH$_3$)$_2$**. (b) Solid-state structures of **Ru-NH$_3$**, **Ru-(NH$_3$)(DMSO)**, **Ru-(NH$_3$)(CH$_3$CN)-O**, **Ru-(NH$_3$)$_2$-O**, and **Ru-(NH$_3$)$_2$-N** determined by X-ray diffraction. Thermal ellipsoids are displayed at 50% probability. All hydrogen atoms bound to carbon are omitted for the sake of clarity.

chelating bpy ligand has a torsion angle of 15.4(7)° (Figure 1b).

Ru-NH$_3$ has poor solubility in acetonitrile. By addition of 2% trifluoroethanol (TFE) in CD_3CN to assist dissolution, two sets of proton resonances with an intensity ratio of ∼2:1 appeared (Figure S3). ^{1}H NMR and selective-ROESY NMR experiments suggested that this presumably corresponded to two isomers of complex [Ru(pdc-κ-N^{1}O^1)(bpy)(NH$_3$)-(CD$_3$CN)] (**Ru-(NH$_3$)(CD$_3$CN)**), named as **Ru-(NH$_3$)-(CD$_3$CN)-N** (the CD_3CN ligand ligates trans to the N atom of the pdc^{2-} ligand, δ_H 2.18 ppm) and **Ru-(NH$_3$)(CD$_3$CN)-O** (the CD_3CN ligand ligates trans to the O atom of the pdc^{2-} ligand, δ_H 2.21 ppm), respectively (Figures S3 and S4). Single crystals grown in CH_3CN gave the isomer **Ru-(NH$_3$)-(CH$_3$CN)-O**, and multiple attempts to separate isomer **Ru-(NH$_3$)(CH$_3$CN)-N** failed probably because of the non-dominant configuration. X-ray diffraction study of **Ru-(NH$_3$)-(CH$_3$CN)-O** showed that the length of Ru−N3 is 2.122(6) Å, similar to the Ru−N3 (2.120(4) Å) of **Ru-(NH$_3$)(DMSO)**, but shorter than the Ru−N3 (2.140(7) Å) of **Ru-NH$_3$**. A hydrogen-bonding interaction is evident between the dangling carboxylate and the incoming NH_3 ligand, exhibiting an N3···O1 distance of 2.955 Å.

Upon adding 400 equiv of NH_3 to a CH_3CN solution of **Ru-NH$_3$**, the stronger σ-donating NH_3 displaced the CH_3CN ligand of **Ru-(NH$_3$)(CH$_3$CN)** to form **Ru-(NH$_3$)$_2$** within 3 h, and a color change from amber to red was observed. This transformation process was monitored by a variable time ^{1}H NMR experiment (Figure S5). Via structural assignments and detailed analysis of ^{1}H NMR, ^{1}H−^{1}H COSY, ^{1}H−^{15}N HSQC, and ^{1}H−^{1}H ROESY spectra of the reaction product, we confirmed the formation of two new isomers **Ru-(NH$_3$)$_2$-N** (NH_3 ligand ligates trans to the N atom of pdc^{2-} ligand) and **Ru-(NH$_3$)$_2$-O** (the NH_3 ligand ligates trans to the O atom of the pdc^{2-} ligand), both of which have an additional amino group coordinating to Ru (Figures S6−S10). Two doublets observed at δ_H 1.82 ppm ($^1J_{15N\text{-}1H}$ = 68.7 Hz) and δ_H 2.01 ppm ($^1J_{15N\text{-}1H}$ = 68.3 Hz) in the ^{1}H NMR spectrum were assigned to the bound $^{15}NH_3$ ligands of the two isomers. The 2D ^{1}H−^{15}N HSQC spectrum displays their cross peaks at δ_H 1.82 ppm and δ_N −49.2 ppm and δ_H 2.01 ppm and δ_N −39.9 ppm, and 2D ROESY correlations at δ_H 1.82/δ_H 3.13 ppm and δ_H

https://doi.org/10.1021/jacsau.5c00054
JACS Au 2025, 5, 1812−1821

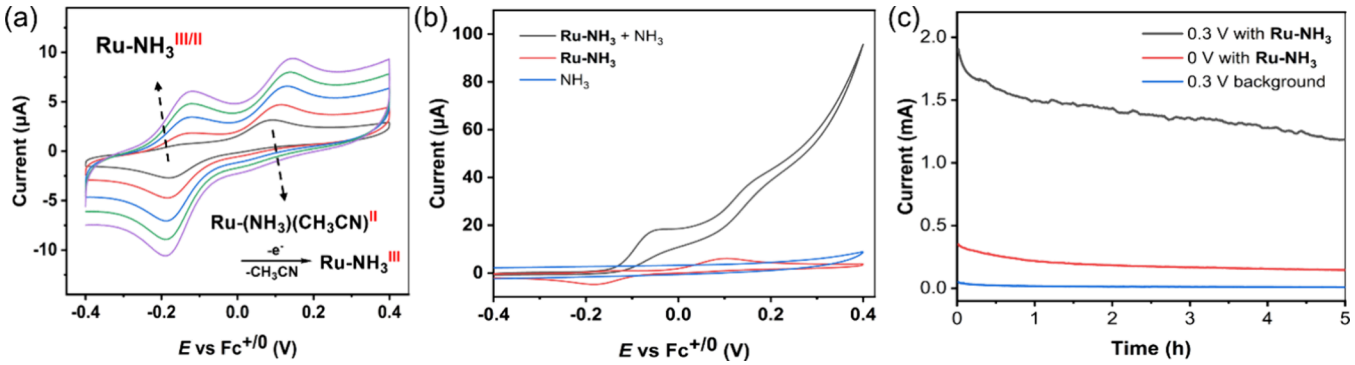

Figure 2. (a) Cyclic voltammograms of 0.5 mM **Ru-NH$_3$** at variable scan rates: 100 (black), 250 (red), 500 (blue), 750 (green), and 1000 mV/s (purple). (b) Cyclic voltammograms of background ammonia oxidation in the presence of 0.2 M NH_3 (blue), 0.5 mM **Ru-NH$_3$** in the absence of NH_3 (red), and ammonia oxidation by 0.5 mM **Ru-NH$_3$** with 0.2 M NH_3 (black). (c) Controlled potential electrolysis of **Ru-NH$_3$** at different applied potentials. 0.5 mM **Ru-NH$_3$** and 0.2 M NH_3 at 0.3 V vs $Fc^{+/0}$ (black), 0 V vs $Fc^{+/0}$ (red), and 0.2 M NH_3 without catalyst at 0.3 V vs $Fc^{+/0}$ (blue). CVs were recorded with a glassy carbon electrode (0.07 cm^2), a Pt counter electrode, and an $Ag/[Ag(NH_3)_2]NO_3$ reference electrode (homemade, for details, see the SI). All acetonitrile solutions contained 2% TFE and 0.1 M $[Bu_4N][PF_6]$.

2.01/δ_H 3.26 ppm were observed, further corroborating this assignment.

Furthermore, the molecular structure of isomer **Ru-$(NH_3)_2$-O** was successfully characterized by the X-ray diffraction experiment (Figure 1b). The dissociation of the carboxylate moiety results in a large N3−Ru−N4 angle (103.45(9)°). The two NH_3 ligands bind to the Ru center with Ru−N3 and Ru−N5 bond lengths of 2.127(2) and 2.151(2) Å, and both construct hydrogen bonds with the pendant carboxylate moieties. Attempts to isolate isomer **Ru-$(NH_3)_2$-N** were made by carefully selecting different crystals. Although the unsatisfactory crystal quality would not diffract to a resolution below 1 Å, the low-resolution crystal structure unequivocally confirmed the identity of the isomer **Ru-$(NH_3)_2$-N**. The molecular structure of isomer **Ru-$(NH_3)_2$-N** is of significant difference in contrast to **Ru-$(NH_3)_2$-O**, which means that the incoming NH_3 ligand ligates trans to the N4 atom of the pdc^{2-} ligand and no hydrogen bond is observed between the pendent carboxylate moiety and the two NH_3 ligands. The N3−N5 length (3.054 Å) between two NH_3 ligands is slightly longer than that of **Ru-$(NH_3)_2$-O** (2.987 Å), which agrees well with the greater intensity of ROESY cross peaks between the two amino ligands (δ_H 3.13 ppm and δ_H 1.82 ppm for **Ru-$(NH_3)_2$-O**) than that between the other two amino ligands (δ_H 3.26 ppm and δ_H 2.01 ppm for **Ru-$(NH_3)_2$-N**).

Electrochemistry of Complex [Ru(pdc-κ-N^{1}O^2)(bpy)(NH$_3$)] (Ru-NH$_3$)

The redox properties of **Ru-NH$_3$** in CH_3CN were studied by cyclic voltammograms at different scan rates in Figure 2a. Note again that **Ru-NH$_3$** in anhydrous acetonitrile leads to **Ru-$(NH_3)(CH_3CN)$**. At a scan rate of 100 mV/s, an irreversible oxidation peak appears at 0.09 V vs $Fc^{+/0}$, which we attributed to the **Ru^{III}-$(NH_3)(CH_3CN)$/Ru^{II}-$(NH_3)(CH_3CN)$** process. This is confirmed by our DFT calculations, which gave a potential of 0.08 V for this one-electron oxidation. This irreversible redox event suggested that a chemical reaction occurs once **Ru^{II}-$(NH_3)(CH_3CN)$** is oxidized to Ru^{III}. Because the O atom is a harder base than the N atom when **Ru^{II}-$(NH_3)(CH_3CN)$** reaches Ru^{III}, the pendent carboxylate arm recoordinating to the Ru center is more favored, concomitant with the dissociation of the solvent CH_3CN ligand to form **Ru^{III}-NH$_3$**. This phenomenon is common in related catalysts for water oxidation reactions.[34,35] Such dissociation was computed to be exergonic by 12.3 kcal/mol from our DFT calculations. On the reverse scan, a cathodic wave appears at −0.19 V vs $Fc^{+/0}$, which was tentatively assigned to the reduction of **Ru^{III}-NH$_3$** to **Ru^{II}-NH$_3$**. Our DFT calculations gave a potential of −0.29 V vs $Fc^{+/0}$ for this one-electron reduction. Compared to the fast scan rate (100 to 1000 mV/s), the relatively slow reaction rate between electrogenerated **Ru^{II}-NH$_3$** and CH_3CN makes the anodic wave at −0.12 V vs $Fc^{+/0}$ reversible. Likewise, the electrochemical behavior of **Ru-NH$_3$** in DMSO also showed the recoordination of the carboxylate ligand when the harder acid Ru^{III} formed (Figure S11).

Electrocatalytic Ammonia Oxidation

Upon adding NH_3 into the CH_3CN solution, two new redox features present at −0.06 and 0.14 V vs $Fc^{+/0}$, respectively, in Figure 2b. The first oxidation peak at −0.06 V was tentatively attributed to **Ru^{II}-$(NH_3)_2$** to **Ru^{III}-$(NH_3)_2$**, which was also consistent with our calculated result of −0.10 V (Figure S34). Once **Ru^{III}-$(NH_3)_2$** forms, it can be converted into the complex Ru^{III}(pdc-κ-N^{1}O^2)(bpy)(NH_3) (**Ru^{III}-NH$_3$**), which may drive the reaction at a low rate (see below for more details.) Although we are currently unable to attribute the redox feature at 0.14 V, a prominent enhancement of catalytic current is observed afterward, indicating that the reaction takes another pathway at higher potential. To simplify the problem, all discussions below focus on the catalytic process at high potential (0.4 V vs $Fc^{+/0}$), unless otherwise noted. Kinetics analysis was conducted by examining the CV response as a function of the catalyst and the ammonia concentration. The catalytic current increases linearly with respect to [**Ru-NH$_3$**] and $[NH_3]^{1/2}$, revealing that the reaction is first order in both [**Ru-NH$_3$**] and $[NH_3]$ (Figures S12 and S13). These observations suggest that **Ru-NH$_3$** initiates the electrocatalytic oxidation of ammonia.

$$E = -0.942 - 0.0789\lg[NH_3] + 0.0592\lg[NH_4^+] \quad (1)$$

$$\frac{i_{plateau}}{i_p} = \frac{n}{0.4463}\sqrt{\frac{RTk_{obs}}{F\upsilon}} \quad (2)$$

Given that the practical electrode potential of AOR in acetonitrile under nonstandard conditions depends on the concentration of ammonium, 0.05 M NH_4PF_6 was added into the solution to obtain the overpotential.[36,37] A calculated

https://doi.org/10.1021/jacsau.5c00054
JACS Au 2025, 5, 1812−1821

overpotential of 0.85 V is achieved by employing eq 1, which corresponds to the low rate catalysis near the initial onset potential of −0.11 V vs $Fc^{+/0}$ (Figure S14). To estimate a catalytic rate (k_{obs}), an approximate model for the pseudo-first-order catalytic system is applied.[38,39] In eq 2, $i_{plateau}$ is the catalytic plateau current, i_p is the noncatalytic peak current in the absence of NH_3, n is the number of transferred electrons (6 for AOR), R is the ideal gas constant, F is Faraday's constant, T is the temperature, and ν is the scan rate. Although this method has only rigorously been verified for simple EC′ mechanisms (a simple electron transfer followed by a catalytic process), it can still be useful in an initial assessment of catalyst performance with more complicated or undetermined catalytic mechanisms. Ideally, under pure kinetic conditions without substrate depletion, k_{obs} can be estimated from the plateau current of an S-shaped CV response. In our case, an ideal S-shaped response is not readily achieved, but a plateau region can be approximated at fast scan rates. Accordingly, a k_{obs} = 18.9 s^{-1} value is deduced from eq 2 (Figure S15).

Controlled potential electrolysis (CPE) experiments were conducted to ensure an electrocatalytic AOR promoted by **Ru-NH$_3$**. In a sealable electrolysis cell, CPE was performed by using a 2 cm^2 carbon paper working electrode, a spiral Pt wire counter electrode, and an $Ag/[Ag(NH_3)_2]NO_3$ reference electrode. At a high potential of 0.3 V vs $Fc^{+/0}$, CPE of a 0.5 mM **Ru-NH$_3$** acetonitrile solution containing 0.2 M NH_3 and 2% TFE maintained a high catalytic current in the initial 5 h (Figure 2c). After 32 h, a charge amount of 98.1 C had passed during electrolysis. Analysis of headspace gas via gas chromatography showed that N_2 and H_2 evolved with faradaic efficiencies of 89.8 and 97.8%, respectively. A TON of 76.1 was achieved based on the amount of N_2. An additional experiment under identical conditions without the presence of **Ru-NH$_3$** showed no catalytic activity. To further confirm that catalytic ammonia oxidation by **Ru-NH$_3$** can take place at a low applied potential, CPE was conducted at an applied potential of 0 V vs $Fc^{+/0}$ for 24 h. A total amount of 12.62 C charges had passed, and 9.4 equiv of N_2 was generated with 86.6% faradaic efficiency, which indicated that electrocatalysis has already begun at this stage. According to the Tafel relationship, current often increases with increasing overpotential. However, the significant current difference between 0 and 0.3 V may not be due to the Tafel relationship but to the different mechanisms operating at different potentials (Figure 2c).

Furthermore, a rinse test was carried out to exclude the possibility of catalysis arising from the heterogeneous species (Figure S17). After CPE, the carbon paper electrode was rinsed with dry CH_3CN thoroughly and was reinserted into a fresh NH_3-CH_3CN solution. No catalytic current was observed, implying that homogeneous **Ru-NH$_3$** worked as the active species during catalysis. When CPE was carried out with **Ru-^{15}NH$_3$** and $^{15}NH_3$, the gas products were detected by GC-MS. The formation of $^{30}N_2$ confirmed that the nitrogen produced originates from ammonia oxidation (Figure S21). Other possible anodic products (NO_2^-, NO_3^-, and N_2H_4) in the electrolyte were not detected by chemical titration method (Figures S22−S27).[19,26,40]

Mechanism Investigation

Based on the CVs analysis, we believed that recoordination of the pendent carboxylate moiety to the Ru center occurred once **Ru^{II}-(NH$_3$)(S)(S = CH$_3$CN/DMSO)** was oxidized to Ru^{III}. DFT calculations[41] confirmed that the transformation of **Ru^{II}-(NH$_3$)(S)** to **Ru^{III}-NH$_3$** is a downhill process (−17.3 kal/mol, Figure S34). The reduction potential of the **Ru^{III}-(NH$_3$)(S)**/**Ru^{II}-(NH$_3$)(S)** couple was calculated to be 0.08 V, and the dissociation of the acetonitrile molecule from **Ru^{III}-(NH$_3$)(S)** is exergonic by 12.3 kcal/mol. Accordingly, we speculated that **Ru^{II}-(NH$_3$)$_2$** underwent a similar process to generate **Ru^{III}-NH$_3$**, accompanied by the dissociation of an ammonia ligand. The calculations showed that one-electron oxidation of **Ru^{II}-(NH$_3$)$_2$** is associated with a potential of −0.10 V, and the dissociation of an ammonia ligand from **Ru^{III}-(NH$_3$)$_2$** is exergonic by 6.7 kcal/mol. To validate the plausible **Ru^{III}-NH$_3$** species, a stoichiometric chemical oxidation experiment was examined. Upon treatment of **Ru-(NH$_3$)$_2$** with one equivalent $FcPF_6$ in acetonitrile, a black solid was obtained with an 87% yield. HR-MS measurements showed that an m/z value of 440.0061 fitted exactly to the simulated value (440.0091), confirming the existence of **Ru^{III}-NH$_3$** species (Figure 3).

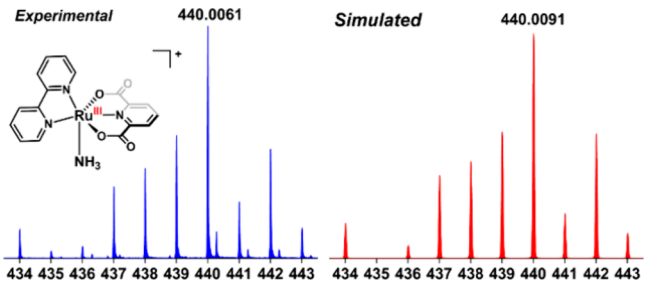

Figure 3. HR-MS spectra of **Ru^{III}-NH$_3$**, experimental (blue) and simulated (red).

The elementary steps involved in the electrochemical ammonia oxidation reaction were explored using DFT calculations to gain more insight into the catalytic mechanism, and the calculated Gibbs energy diagram is displayed in Figures 4 and 5. A reference potential of 0.3 V (vs $Fc^{+/0}$) in the CPE was used to set up the energy diagram. During oxidation, the proton is released into the solution and captured by ammonia molecules, forming an ammonium ($[NH_4{\bullet}{\bullet}{\bullet}NH_3]^+$) cation. Therefore, a pH of 15.1 was applied, corresponding to the pK_a of an ammonium ($[NH_4{\bullet}{\bullet}{\bullet}NH_3]^+$) cation in acetonitrile. The whole reaction was calculated to be exergonic by 141.5 kcal/mol as the potential for ammonia oxidation was calculated to be −0.723 V at pH = 15.1 (0.170 V at pH = 0). Starting from the **Ru^{II}−NH$_3$** complex (labeled as **^{1}1**, Ru−N distance of 2.17 Å), one-electron oxidation (potential of −0.29 V) with the electron released from the metal center takes place to generate the **Ru^{III}−NH$_3$** complex **^{2}2** (Ru−N distance of 2.17 Å), in which the spin population on Ru is 0.82. From **^{2}2**, removing a proton and an electron is associated with a potential of 0.79 V, leading to a **Ru^{IV}−NH$_2$** complex **^{1}3** (Ru−N distance of 1.87 Å). The subsequent oxidation of **^{1}3** to generate **^{2}4** is a two-proton coupled electron transfer process with a potential of 0.07 V, which is even lower than the oxidation of **^{2}2**. The pK_as of **Ru^{V}−NH$_2$** and **Ru^{V}=NH** were calculated to be −2.5 and 3.0, respectively, suggesting that both protons are released into the solution during the oxidation. In **^{2}4**, the spin populations on Ru and N1 are 0.15 and 0.77, respectively. The electronic structure of **^{2}4** (**Ru^{IV}=N•**, Ru−N distance of 1.70 Å) can thus be described as low-spin Ru^{IV} (S_{Ru} = 0) interacting with a nitrogen radical (S_N = 1/2). Furthermore, one-electron oxidation of **^{2}4** to produce a **Ru^{VI}≡N** complex **^{1}5** (Ru−N

https://doi.org/10.1021/jacsau.5c00054
JACS Au 2025, 5, 1812−1821

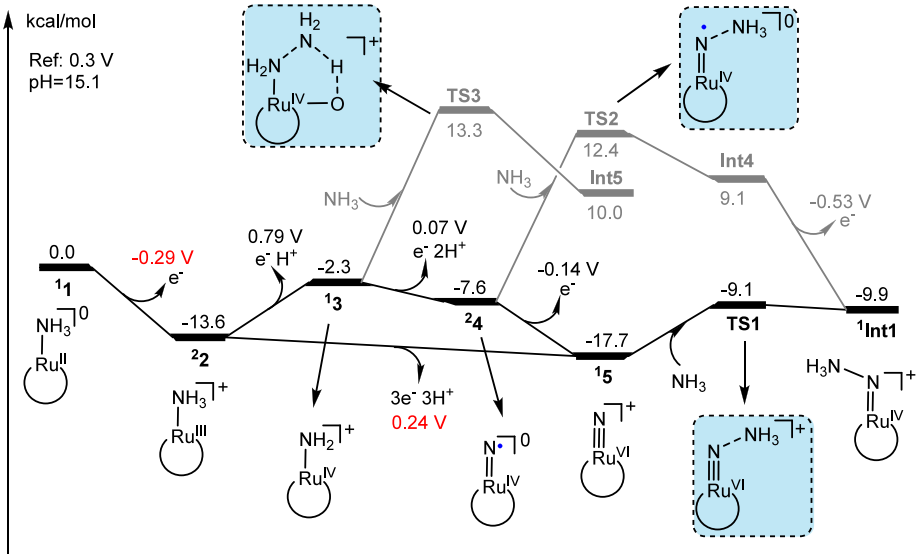

Figure 4. Gibbs energy diagram (in kcal/mol) for NH_3 oxidation processes in CH_3CN. An applied potential of 0.3 V vs $Fc^{+/0}$ and pH = 15.1 were used to calculate the thermodynamics for every oxidation steps. The left superscript indicates the spin multiplicity of the species.

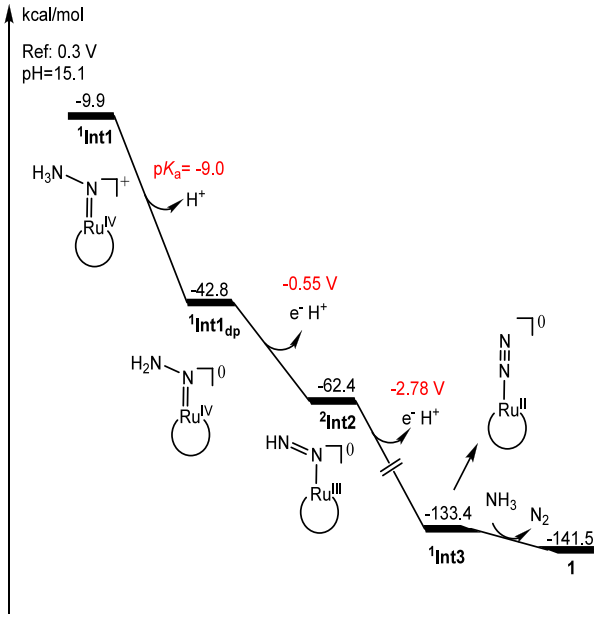

Figure 5. Gibbs energy diagram (in kcal/mol) for N_2 release processes in CH_3CN. An applied potential of 0.3 V vs $Fc^{+/0}$ and pH = 15.1 were used to calculate the thermodynamics for every oxidation step. The left superscript indicates the spin multiplicity of the species.

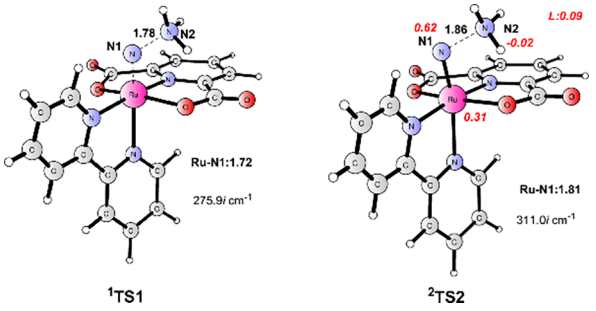

Figure 6. Optimized transition states for N−N bond formation at the Ru^{VI} (**TS1**) and Ru^{V} (**TS2**) states. Distances are given in angstrom, spin populations are presented in red italics, and the imaginary frequency for each transition state is shown.

distance of 1.61 Å) has a potential of −0.14 V. The calculations thus suggested that the oxidative conversion of ^{2}**2** to ^{1}**5** may proceed concomitantly with the release of three electrons and three protons, with a potential of 0.24 V. This potential is slightly lower than the applied potential of 0.3 V, suggesting that the formation of ^{1}**5** is exergonic.

^{1}**5** could react with one ammonia molecule by forming one N−N bond, and the transition state for this step (**TS1**) is shown in Figure 6. **TS1** was calculated to have a barrier of 8.6 kcal/mol relative to ^{1}**5** plus an NH_3 molecule. In **TS1**, the nascent N1−N2 bond distance is 1.78 Å and the Ru−N1 bond distance is 1.72 Å. During the N−N bond formation, two electrons are delivered from the ammonia group to the metal center, which is reduced to Ru^{IV} in **Int1**. Importantly, deprotonation of the ammonia group is not needed for the present N−N bond formation process. This mechanism is similar to the suggested mechanism for other Ru-catalyzed ammonia oxidation, in which Ru≡N is used for N−N bond formation.[32,42,43] When neutral nitrogen-based ligands were used, Ru^{IV}=NH was suggested to be the key oxidant for N−N bond formation.[9] Furthermore, during ammonia oxidation using first-row transition metal complexes, an M-NH_2 species is commonly formed, which leads to either an ammonia attack or a biomolecular coupling.[11,20] The pK_a of the resulting intermediate ^{1}**Int1** (formally **Ru^{IV}=N-NH_3^+**) was calculated to be −9.0, suggesting that ^{1}**Int1** prefers to release a proton to form ^{1}**Int1dp** (**Ru^{IV}=N-NH_2**) with an energy release of 32.9 kcal/mol (Figure 5). From ^{1}**Int1dp**, removing a proton and an electron to generate **Ru^{III}−N = NH** complex ^{2}**Int2** (Ru−N distance of 1.21 Å) is associated with a potential of −0.55 V, with an energy release of 19.6 kcal/mol (Figure 5). The proton and an electron are both from the −NH_2 group, and an intramolecular electron transfer from the NNH moiety to the Ru^{IV} center takes place to generate Ru^{III} complex ^{2}**Int2**. Further PCET oxidation of ^{2}**Int2** (potential of −2.78 V) results in the production of dinitrogen-coordinated Ru^{II} complex ^{1}**Int3**. The release of one H atom from the −NH moiety of ^{2}**Int2** leads to a shorter N−N bond in ^{1}**Int3** (N−N distance of 1.12 Å). Similarly to the previous oxidation step,

https://doi.org/10.1021/jacsau.5c00054
JACS Au 2025, 5, 1812−1821

intramolecular electron transfer occurs from the NN moiety to the metal. Eventually, the ligand exchange of N_2 by NH_3 regenerates ^{1}**1** for the next catalytic cycle.

The calculations suggested that the critical N−N bond formation requires access to the highly valent Ru^{VI} state. N−N bond formation has also been considered at the formal Ru^{V} state via **TS2** and at the formal Ru^{IV} state via **TS3**. However, the barrier of **TS2** is 20.0 kcal/mol relative to that of ^{2}**4** plus NH_3 or 30.1 kcal/mol relative to that of ^{1}**5** plus NH_3. Furthermore, **TS3** is associated with a barrier of 15.6 kcal/mol, which is also higher than that of **TS1**. It should be noted that further one-electron oxidation of the Ru^{VI} complex is not possible, as its potential was calculated to be as high as 2.80 V.

CONCLUSIONS

In summary, we described electrocatalytic ammonia oxidation to N_2 by the complex [Ru(pdc-κ-N^1O^2)(bpy)(NH_3)] (**Ru-NH_3**) at a mild potential. Experimental and theoretical investigations indicated that the oxidation of **Ru-NH_3** affords a **Ru^{III}−NH_3** intermediate, which can undergo three sequential electron and proton transfer steps to give a **Ru^{VI}≡N** species. We suggested that N−N bond formation occurs upon ammonia attack of this **Ru^{VI}≡N** species. On the other hand, the catalysis observed at a low potential of 0 V vs $Fc^{+/0}$ may suggest another catalytic mechanism. We speculated that **Ru−N_2H_4** analogues might be generated, as high-valent species are not required at low applied potentials. The oxidation of hydrazine eventually leads to N_2. Studies are underway to experimentally decipher these two different catalytic mechanisms.

In this molecular system, the anionic nature of the pdc^{2-} ligand significantly reduces the overpotential of ammonia oxidation and stabilizes Ru in high oxidation states. The labile carboxylate moieties, however, also led to the formation of various **Ru-(NH_3)(S)(S = CH_3CN/DMSO/NH_3)** species. This study emphasizes the importance of ligand selection, i.e., how to sustain the catalytic activity while decreasing the overpotential. Future efforts are aimed at controlling the opening process of the carboxylate moiety to avoid the unnecessary structural transformation.

METHODS

General

NMR. All NMR experiments were performed at 25 °C on a Bruker NEO 600 MHz NMR spectrometer (600.23 MHz for proton frequency) equipped with a QCI-F Cryoprobe. Chemical shifts (δ) were reported in parts per million with the solvent resonance as the internal standard.

Gas Chromatography (GC) and GC-MS Methods. Evolved nitrogen gas was quantified with a gas chromatograph (FULI 9790PLUS) equipped with a modified Porapak Q (2m × 4 mm 60−80 mesh), a 5 Å molecular sieve column (3 m × 4 mm 60−80 mesh), and a thermal conductivity detector. Argon was used as the carrier gas. Standard curves were generated by the direct injection of known volumes of hydrogen or nitrogen gas. Quantification of the background nitrogen was determined using the background oxygen signal. Isotopic N_2 formation was detected by mass spectrometry with a Thermo Scientific ISQ 7000 single quadrupole mass spectrometer using helium as the carrier gas.

Mass Spectra (MS) and High-Resolution Mass Spectra (HR-MS). MS and HR-MS were performed with a Q-Tof Micro and Synapt G2-Si HDMS mass spectrometer, respectively.

UV−Vis. The UV−vis spectra were collected by using a PerkinElmer spectrophotometer.

X-ray Crystallography. X-ray crystallographic analyses were recorded on a Bruker D8 Venture diffractometer with a PHOTON II detector in shutterless mode with an incoat microfocus source (Mo K_α radiation, λ = 0.71073 Å or Cu K_α radiation, λ = 1.54178 Å) equipped with an Oxford 800 Plus liquid nitrogen vapor cooling device. All the data were collected at 301 or 100 K. The computing indexing, cell refinement, and data reduction were processed using APEX4 software. All data were integrated with SAINT, and a multiscan absorption correction using SADABS was applied. The structure was solved by dual methods using SHELXT and refined by full-matrix least-square methods against F^2 by SHELXL.

Electrochemistry. All electrochemical experiments were measured with a CHI 660e electrochemical workstation (Shanghai Chen Hua Instrument Co., Ltd.) using a one-compartment, three-electrode custom-built cell (56 mL). For CVs, a glassy carbon disk electrode (A = 0.07 cm^2), a Pt wire, and an Ag/[$Ag(NH_3)_2$]NO_3 reference electrode (homemade) were used as the working, counter, and auxiliary electrodes, respectively. Since testing under environmental conditions has no significant impact on test results compared with testing under inert gas protection, all CV tests were performed under environmental conditions for convenience. For CPE, the same reference electrode was used, but a carbon paper (geometric area: 2 cm^2) and a spiral Pt wire were used as the working and counter electrodes. The sealed electrolytic cell was purged with argon for 20 min before each CPE test to eliminate residual air. All redox potentials are reported versus the $Fc^{+/0}$ couple in this work.

Synthesis and Materials

All reactions were performed using standard Schlenk or glovebox techniques under a nitrogen or argon atmosphere, unless otherwise noted. All reagents were purchased from commercial sources and used without further purification unless otherwise mentioned. All solvents were dried by general methods and degassed before use. Research-grade NH_3 gas of 99.999% purity was purchased from Air Liquide and used as received. Anhydrous ammonia gas was dried by passage through a calcium oxide drying tube. ^{15}N-labeled ammonia gas (98 atom % ^{15}N) was purchased from Cambridge Isotope Laboratories. Super-dry acetonitrile with molecular sieves (99.9%) was purchased from J&KSeal. 2,2,2-Trifluoroethanol (99.9%) was purchased from Innochem. Ferrocenium hexafluorophosphate (98%) was purchased from Yuanye. Ruthenium trichloride trihydrate, dipicolinic (H_2pdc) acid, and 2,2′-bipyridine (bpy) were purchased from Picasso, Leyan, and TCI, respectively. [Bu_4N]PF_6 (tetrabutylammonium hexafluorophosphate, 99%+) was purchased from Adamas-beta. To ensure its purity, the electrolyte was further recrystallized in a hot ethanol solution, and the resulting needle crystals were rigorously vacuum-dried for several days to remove the residual solvents.

Synthesis of Ru(pdc-κ-N^1O^2)(bpy)Cl (Ru−Cl)

Ru(pdc-κ-N^1O^2)(bpy)Cl was prepared as reported previously.[33]

Synthesis of Ru(pdc-κ-N^1O^2)(bpy)(NH_3) (Ru-NH_3)

Ru(pdc-κ-N^1O^2)(bpy)Cl (200 mg, 0.44 mmol) was suspended in CH_3OH/H_2O (80 mL/20 mL), and $AgPF_6$ (110 mg, 0.44 mmol) was added. The suspension was heated to a reflux temperature for 2 h. Then, an excess of aqueous ammonia (20 mL) was added. The solution immediately changed to dark red, and the resulting mixture was refluxed for another 2 h. After 2 h, the solution was then allowed to cool to room temperature and filtered to remove the AgCl precipitate. The filtrate was evaporated to dryness. The resulting mixture was purified by chromatography on alumina with CH_3OH/CH_2Cl_2 (1/5 to 2/5) as eluent. The first red bend was attained as the desired product **Ru-NH_3**. The second red bend belonged to complex [Ru(pdc-κ-N^1O^1)(bpy)(NH_3)$_2$] (Ru-(NH_3)$_2$), which was not stable on an alumina column and would gradually convert to **Ru-NH_3** without ammonia protection. Thus, attempts to isolate pure **Ru-(NH_3)$_2$** failed. The black solid of **Ru-NH_3** was recrystallized from CH_3OH/Et_2O to provide a red crystal for X-ray crystallography. ESI-HR-MS: calcd for $C_{17}H_{14}N_4O_4Ru$ + H, 441.0141; found, 441.0138. ^{1}H NMR (600 MHz, CD_3OD) δ = 9.60 (d, J = 5.6, 1H), 8.68 (d, J = 8.2, 1H), 8.52 (d, J = 8.1, 1H), 8.22 (d, J = 7.8, 2H), 8.09 (t, J = 7.8,

https://doi.org/10.1021/jacsau.5c00054
JACS Au 2025, 5, 1812−1821

1H), 8.00 (t, 1H), 7.74 (m, 2H), 7.44 (d, 1H), 7.26 (t, 1H), proton signals of NH_3 ligand overlaps with CD_3OD.

Synthesis of Ru(pdc-κ-N^1O^2)(bpy)($^{15}NH_3$) (Ru−$^{15}NH_3$)

The synthesis of complex **Ru−^{15}NH$_3$** is similar to that of complex **Ru-NH$_3$**. Ru(pdc-κ-N^1O^2)(bpy)Cl (50 mg, 0.11 mmol) was suspended in CH_3OH/H_2O (20 mL/5 mL), and $AgPF_6$ (27.5 mg, 0.11 mmol) was added. The suspension was heated to reflux temperature for 2 h. Then, the reaction solution was bubbled with ^{15}N-labeled ammonia gas until it changed to dark red. The resulting mixture was refluxed for another 2 h. After that, the solution was allowed to cool to room temperature and filtered to remove AgCl precipitate. The filtrate was evaporated to dryness and further purified by chromatography on alumina.

Synthesis of [Ru^{III}(pdc-κ-N^1O^2)(bpy)(NH_3)](PF_6) (Ru^{III}−NH_3)

RuII(pdc-κ-N^1O^2)(bpy)(NH_3) (5 mg, 0.011 mmol) was dissolved in CH_3CN (5 mL, containing 5% TFE) and bubbled with excess ammonia gas. The resulting solution was left for 1 day to completely convert to **Ru-$(NH_3)_2$**. The solution was treated with 1 equiv of $FcPF_6$ (3.8 mg, 0.011 mmol) and stirred for 30 min at −35 °C. After reaction, excess cold diethyl ether was added to the system, and the solution was kept stationary for 2 h to obtain a dark-red precipitate (yield 87%).

■ ASSOCIATED CONTENT

Supporting Information

The Supporting Information is available free of charge at https://pubs.acs.org/doi/10.1021/jacsau.5c00054.

All the characterization data: NMR spectra, HR-MS spectra, and crystal data for complexes mentioned in this article; experimental and computational details, materials, and methods; and photographs of experimental setup (DOCX)

Accession Codes

CCDC 2371169−2371172, 2371287 contain the supplementary crystallographic data for this paper. These data can be obtained free of charge via www.ccdc.cam.ac.uk/data_request/cif, or by emailing data_request@ccdc.cam.ac.uk, or by contacting The Cambridge Crystallographic Data Centre, 12 Union Road, Cambridge CB2 1EZ, UK; fax: + 44 1223 336033.

■ AUTHOR INFORMATION

Corresponding Authors

Rongzhen Liao − *Key Laboratory of Material Chemistry for Energy Conversion and Storage, Ministry of Education, Hubei Key Laboratory of Bioinorganic Chemistry and Materia Medica, Hubei Key Laboratory of Materials Chemistry and Service Failure, School of Chemistry and Chemical Engineering, Huazhong University of Science and Technology, Wuhan 430074, China;* orcid.org/0000-0002-8989-6928; Email: rongzhen@hust.edu.cn

Biaobiao Zhang − *Center of Artificial Photosynthesis for Solar Fuels and Department of Chemistry, School of Science and Research Center for Industries of the Future, Westlake University, Hangzhou, Zhejiang 310024, China; Institute of Natural Sciences, Westlake Institute for Advanced Study, Hangzhou, Zhejiang 310024, China; Division of Solar Energy Conversion and Catalysis at Westlake University, Zhejiang Baima Lake Laboratory Co., Ltd., Hangzhou, Zhejiang 310000, China;* orcid.org/0000-0002-4093-1251; Email: zhangbiaobiao@westlake.edu.cn

Authors

Jun Li − *Department of Chemistry, Zhejiang University, Hangzhou, Zhejiang 310058, China; Center of Artificial Photosynthesis for Solar Fuels and Department of Chemistry, School of Science and Research Center for Industries of the Future, Westlake University, Hangzhou, Zhejiang 310024, China; Institute of Natural Sciences, Westlake Institute for Advanced Study, Hangzhou, Zhejiang 310024, China*

Xiaohuo Shi − *Key Laboratory of Precise Synthesis of Functional Molecules of Zhejiang Province, Instrumentation and Service Center for Molecular Sciences, Westlake University, Hangzhou, Zhejiang 310024, China*

Feiyang Zhang − *Department of Chemistry, Zhejiang University, Hangzhou, Zhejiang 310058, China; Center of Artificial Photosynthesis for Solar Fuels and Department of Chemistry, School of Science and Research Center for Industries of the Future, Westlake University, Hangzhou, Zhejiang 310024, China; Institute of Natural Sciences, Westlake Institute for Advanced Study, Hangzhou, Zhejiang 310024, China*

Xingyu Lu − *Key Laboratory of Precise Synthesis of Functional Molecules of Zhejiang Province, Instrumentation and Service Center for Molecular Sciences, Westlake University, Hangzhou, Zhejiang 310024, China*

Yaqiong Zhang − *Hubei Key Laboratory of Purification and Application of Plant Anti-Cancer Active Ingredients, College of Chemistry and Life Science, Hubei University of Education, Wuhan 430205, China;* orcid.org/0000-0002-6809-5910

Complete contact information is available at: https://pubs.acs.org/10.1021/jacsau.5c00054

Author Contributions

B.Z. supervised this project; J.L. performed experiments and wrote the manuscript. X.S. and X.L. performed the NMR experiments; Y.Z. and R.L. performed the computational calculations; F.Z. contributed to the discussion of the paper.

Notes

The authors declare no competing financial interest.

■ ACKNOWLEDGMENTS

This work is financially supported by the National Key R&D Program of China (2022YFC3401802), the National Natural Science Foundation of China (22279105), the Zhejiang Provincial Natural Science Foundation (XHD24B0201), the starting-up package from Westlake University, and the Kunpeng research fund from Zhejiang Province, Research Center for Industries of The Future, and Zhejiang Baima Lake Laboratory. We thank Instrumentation and Service Center for Molecular Sciences and Instrumentation and Service Center for Physical Sciences at Westlake University for the facility support and technical assistance. We thank the Center of Artificial Photosynthesis (CAP) for Solar Fuels at Westlake University for academic and instrument support. We thank Dr. Fu-Cheng Leng and Yuan−Yuan Cai for assisting with collecting the XRD structural data, Kai Guo for analyzing the XRD structural data, and Dr. Rui Zhang for her help, encouragement, and meaningful discussions. We also thank Dr. Rong Zhang from Dalian University of Technology for the MS measurement and discussion.

REFERENCES

(1) MacFarlane, D. R.; Cherepanov, P. V.; Choi, J.; Suryanto, B. H. R.; Hodgetts, R. Y.; Bakker, J. M.; Ferrero Vallana, F. M.; Simonov, A. N. A Roadmap to the Ammonia Economy. *Joule.* **2020**, *4*, 1186−1205.

(2) Valera-Medina, A.; Amer-Hatem, F.; Azad, A. K.; Dedoussi, I. C.; de Joannon, M.; Fernandes, R. X.; Glarborg, P.; Hashemi, H.; He, X.; Mashruk, S.; McGowan, J.; Mounaim-Rouselle, C.; Ortiz-Prado, A.; Ortiz-Valera, A.; Rossetti, I.; et al. Review on Ammonia as a Potential Fuel: From Synthesis to Economics. *Energy Fuels* **2021**, *35*, 6964−7029.

(3) Zhao, Y.; Setzler, B. P.; Wang, J.; Nash, J.; Wang, T.; Xu, B.; Yan, Y. An Efficient Direct Ammonia Fuel Cell for Affordable Carbon-Neutral Transportation. *Joule* **2019**, *3*, 2472−2484.

(4) Zhou, B.; Zhang, N.; Wu, Y.; Yang, W.; Lu, Y.; Wang, Y.; Wang, S. An Option for Green and Sustainable Future: Electrochemical Conversion of Ammonia into Nitrogen. *J. Energy Chem.* **2021**, *60*, 384−402.

(5) Rathore, S. S.; Biswas, S.; Fini, D.; Kulkarni, A. P.; Giddey, S. Direct Ammonia Solid-Oxide Fuel Cells: A Review of Progress and Prospects. *Int. J. Hydrog. Energy* **2021**, *46*, 35365−35384.

(6) Dunn, P. L.; Cook, B. J.; Johnson, S. I.; Appel, A. M.; Bullock, R. M. Oxidation of Ammonia with Molecular Complexes. *J. Am. Chem. Soc.* **2020**, *142*, 17845−17858.

(7) Liu, H.-Y.; Lant, H. M. C.; Cody, C. C.; Jelušić, J.; Crabtree, R. H.; Brudvig, G. W. Electrochemical Ammonia Oxidation with Molecular Catalysts. *ACS Catal.* **2023**, *13*, 4675−4682.

(8) Stephens, D. N.; Mock, M. T. Molecular Complexes for Catalytic Ammonia Oxidation to Dinitrogen and the Cleavage of N−H Bonds. *Eur. J. Inorg. Chem.* **2024**, *27*, No. e202400039.

(9) Habibzadeh, F.; Miller, S. L.; Hamann, T. W.; Smith, M. R. Homogeneous Electrocatalytic Oxidation of Ammonia to N_2 under Mild Conditions. *Proc. Natl. Acad. Sci. U.S.A.* **2019**, *116*, 2849−2853.

(10) Chen, C.-P.; Alharbi, W.; Cundari, T. R.; Hamann, T. W.; Smith, M. R. I. Deciphering the Mechanism of Base-Triggered Conversion of Ammonia to Molecular Nitrogen and Methylamine to Cyanide. *J. Am. Chem. Soc.* **2023**, *145*, 26339−26349.

(11) Toda, H.; Kuroki, K.; Kanega, R.; Kuriyama, S.; Nakajima, K.; Himeda, Y.; Sakata, K.; Nishibayashi, Y. Manganese-Catalyzed Ammonia Oxidation into Dinitrogen under Chemical or Electrochemical Conditions. *ChemPlusChem.* **2021**, *86*, 1511−1516.

(12) Zott, M. D.; Garrido-Barros, P.; Peters, J. C. Electrocatalytic Ammonia Oxidation Mediated by a Polypyridyl Iron Catalyst. *ACS Catal.* **2019**, *9*, 10101−10108.

(13) Zott, M. D.; Peters, J. C. Enhanced Ammonia Oxidation Catalysis by a Low-Spin Iron Complex Featuring *Cis* Coordination Sites. *J. Am. Chem. Soc.* **2021**, *143*, 7612−7616.

(14) Li, Y.; Chen, J.-Y.; Miao, Q.; Yu, X.; Feng, L.; Liao, R.-Z.; Ye, S.; Tung, C.-H.; Wang, W. A Parent Iron Amido Complex in Catalysis of Ammonia Oxidation. *J. Am. Chem. Soc.* **2022**, *144*, 4365−4375.

(15) Zott, M. D.; Peters, J. C. Improving Molecular Iron Ammonia Oxidation Electrocatalysts via Substituent Effects That Modulate Standard Potential and Stability. *ACS Catal.* **2023**, *13*, 14052−14057.

(16) Phearman, A. S.; Bullock, R. M. Synthesis and Reactivity of Fe(II) Complexes Containing Cis Ammonia Ligands. *Inorg. Chem.* **2024**, *63*, 2024−2033.

(17) Liu, L.; Johnson, S. I.; Appel, A. M.; Bullock, R. M. Oxidation of Ammonia Catalyzed by a Molecular Iron Complex: Translating Chemical Catalysis to Mediated Electrocatalysis. *Angew. Chem., Int. Ed.* **2024**, *136*, No. e202402635.

(18) Stephens, D. N.; Szilagyi, R. K.; Roehling, P. N.; Arulsamy, N.; Mock, M. T. Catalytic Ammonia Oxidation to Dinitrogen by a Nickel Complex. *Angew. Chem., Int. Ed.* **2023**, *62*, No. e202213462.

(19) Liu, H.-Y.; Lant, H. M. C.; Troiano, J. L.; Hu, G.; Mercado, B. Q.; Crabtree, R. H.; Brudvig, G. W. Electrocatalytic, Homogeneous Ammonia Oxidation in Water to Nitrate and Nitrite with a Copper Complex. *J. Am. Chem. Soc.* **2022**, *144*, 8449−8453.

(20) Ahmed, M. E.; Raghibi Boroujeni, M.; Ghosh, P.; Greene, C.; Kundu, S.; Bertke, J. A.; Warren, T. H. Electrocatalytic Ammonia Oxidation by a Low-Coordinate Copper Complex. *J. Am. Chem. Soc.* **2022**, *144*, 21136−21145.

(21) Bhattacharya, P.; Heiden, Z. M.; Wiedner, E. S.; Raugei, S.; Piro, N. A.; Kassel, W. S.; Bullock, R. M.; Mock, M. T. Ammonia Oxidation by Abstraction of Three Hydrogen Atoms from a Mo−NH_3 Complex. *J. Am. Chem. Soc.* **2017**, *139*, 2916−2919.

(22) Nakajima, K.; Toda, H.; Sakata, K.; Nishibayashi, Y. Ruthenium-Catalysed Oxidative Conversion of Ammonia into Dinitrogen. *Nat. Chem.* **2019**, *11*, 702−709.

(23) Bhattacharya, P.; Heiden, Z. M.; Chambers, G. M.; Johnson, S. I.; Bullock, R. M.; Mock, M. T. Catalytic Ammonia Oxidation to Dinitrogen by Hydrogen Atom Abstraction. *Angew. Chem., Int. Ed.* **2019**, *58*, 11618−11624.

(24) Holub, J.; Vereshchuk, N.; Sánchez-Baygual, F.-J.; Gil-Sepulcre, M.; Benet-Buchholz, J.; Llobet, A. Synthesis, Structure, and Ammonia Oxidation Catalytic Activity of Ru-NH_3 Complexes Containing Multidentate Polypyridyl Ligands. *Inorg. Chem.* **2021**, *60*, 13929−13940.

(25) Trenerry, M. J.; Wallen, C. M.; Brown, T. R.; Park, S. V.; Berry, J. F. Spontaneous N2 Formation by a Diruthenium Complex Enables Electrocatalytic and Aerobic Oxidation of Ammonia. *Nat. Chem.* **2021**, *13*, 1221−1227.

(26) Chen, G.; He, P.; Liu, C.; Mo, X.-F.; Wei, J.-J.; Chen, Z.-W.; Cheng, T.; Fu, L.-Z.; Yi, X.-Y. Direct Synthesis of Hydrazine by Efficient Electrochemical Ruthenium-Catalysed Ammonia Oxidation. *Nat. Catal.* **2023**, *6*, 949−958.

(27) Toda, H.; Kuroki, K.; Kanega, R.; Yano, T.; Yoshikawa, T.; Kuriyama, S.; Himeda, Y.; Sakata, K.; Nishibayashi, Y. Catalytic Ammonia Oxidation Using Ammonia Solution under Electrochemical Conditions: Investigation on Axial Ligand of Ruthenium Catalysts. *Bull. Chem. Soc. Jpn.* **2023**, *96*, 980−988.

(28) Jacob, S. I.; Chakraborty, A.; Chamas, A.; Bock, R.; Sepunaru, L.; Ménard, G. Rapid Aqueous Ammonia Oxidation to N2 Using a Molecular Ru Electrocatalyst. *ACS Energy Lett.* **2023**, *8*, 3760−3766.

(29) Toda, H.; Kanega, R.; Yano, T.; Yoshikawa, T.; Kuriyama, S.; Himeda, Y.; Sakata, K.; Nishibayashi, Y. Electrochemical Ammonia Oxidation Catalyzed by Ruthenium Complexes: Investigation of Substituent Effect of Axial Pyridine Ligands. *Chem. Lett.* **2024**, *53*, No. upae040.

(30) Feng, S.; Chen, J.; Wang, R.; Li, H.; Xie, J.; Guo, Z.; Lau, T.-C.; Liu, Y. Dual Pathways in Catalytic Ammonia Oxidation by a Ruthenium Complex Bearing a Tetradentate Bipyridine−Bipyrazole Ligand: Isolation of a Diruthenium Intermediate with a μ-Hexazene Derivative. *J. Am. Chem. Soc.* **2024**, *146*, 21490−21495.

(31) Zhao, S.; Zhang, X.; Chen, G.; Cheng, T.; Ding, X.-L.; Zhong, S.-D.; Yang, S.-P.; He, P.; Yi, X.-Y. Selective Electrocatalytic Oxidation of Ammonia by Ru-Dpp Complexes Containing Aromatic Nitrogen Donor as Axial Ligand. *Inorg. Chem.* **2024**, *63*, 23150−23157.

(32) Beiler, A. M.; Denisiuk, A.; Holub, J.; Sánchez-Baygual, F.-J.; Gil-Sepulcre, M.; Ertem, M. Z.; Moonshiram, D.; Piccioni, A.; Llobet, A. Heterogeneous Electrochemical Ammonia Oxidation with a Ru-Bda Oligomer Anchored on Graphitic Electrodes via CH−π Interactions. *ACS Energy Lett.* **2023**, *8*, 172−178.

(33) Hoque, M. A.; Benet-Buchholz, J.; Llobet, A.; Gimbert-Suriñach, C. Catalytic Oxidation of Water to Dioxygen by Mononuclear Ru Complexes Bearing a 2,6-Pyridinedicarboxylato Ligand. *ChemSusChem.* **2019**, *12*, 1949−1957.

(34) Matheu, R.; Ertem, M. Z.; Benet-Buchholz, J.; Coronado, E.; Batista, V. S.; Sala, X.; Llobet, A. Intramolecular Proton Transfer Boosts Water Oxidation Catalyzed by a Ru Complex. *J. Am. Chem. Soc.* **2015**, *137*, 10786−10795.

(35) Duan, L.; Wang, L.; Inge, A. K.; Fischer, A.; Zou, X.; Sun, L. Insights into Ru-Based Molecular Water Oxidation Catalysts: Electronic and Noncovalent-Interaction Effects on Their Catalytic Activities. *Inorg. Chem.* **2013**, *52*, 7844−7852.

(36) Li, J.; Zhang, F.; Xiong, H.; Cai, Y.; Zhang, B. Molecular Catalysts for Electrocatalytic Ammonia Oxidation. *Sci. China Chem.* **2024**, *67*, 3976−3993.

https://doi.org/10.1021/jacsau.5c00054
JACS Au 2025, 5, 1812−1821

(37) Lindley, B. M.; Appel, A. M.; Krogh-Jespersen, K.; Mayer, J. M.; Miller, A. J. M. Evaluating the Thermodynamics of Electrocatalytic N_2 Reduction in Acetonitrile. *ACS Energy Lett.* **2016**, *1*, 698−704.
(38) Lee, K. J.; Elgrishi, N.; Kandemir, B.; Dempsey, J. L. Electrochemical and Spectroscopic Methods for Evaluating Molecular Electrocatalysts. *Nat. Rev. Chem.* **2017**, *1*, No. 0039.
(39) Costentin, C.; Savéant, J.-M. Multielectron, Multistep Molecular Catalysis of Electrochemical Reactions: Benchmarking of Homogeneous Catalysts. *ChemElectroChem.* **2014**, *1*, 1226−1236.
(40) Roithmeyer, H.; Sévery, L.; Moehl, T.; Spingler, B.; Blacque, O.; Fox, T.; Iannuzzi, M.; Tilley, S. D. Electrocatalytic Ammonia Oxidation with a Tailored Molecular Catalyst Heterogenized via Surface Host−Guest Complexation. *J. Am. Chem. Soc.* **2024**, *146*, 430−436.
(41) For computational details, see Supporting Information.
(42) Najafian, A.; Cundari, T. R. Computational Mechanistic Study of Electro-Oxidation of Ammonia to N_2 by Homogenous Ruthenium and Iron Complexes. *J. Phys. Chem. A* **2019**, *123*, 7973−7982.
(43) Trenerry, M. J.; Acosta, M.; Berry, J. F. Computational Analysis of Low Overpotential Ammonia Oxidation by Metal−Metal Bonded Ruthenium Catalysts, and Predictions for Related Osmium Catalysts. *J. Phys. Chem. A* **2024**, *128*, 4038−4051.

https://doi.org/10.1021/jacsau.5c00054
JACS Au 2025, 5, 1812−1821